

## SPATIALLY RESOLVED KINEMATICS IN THE CENTRAL 1 KPC OF A COMPACT STAR-FORMING GALAXY AT $z \sim 2.3$ FROM ALMA CO OBSERVATIONS

G. BARRO<sup>1,2</sup>, M. KRIEK<sup>2</sup>, P. G. PÉREZ-GONZÁLEZ<sup>3</sup>, T. DIAZ-SANTOS<sup>4</sup>, S. H. PRICE<sup>5</sup>, W. RUJOPAKARN<sup>6,7,8</sup>, V. PANDYA<sup>9</sup>, D. C. KOO<sup>9</sup>, S. M. FABER<sup>9</sup>, A. DEKEL<sup>10</sup>, J. R. PRIMACK<sup>11</sup>, D. D. KOCEVSKI<sup>12</sup>

*Last edited: December 6, 2017*

### ABSTRACT

We present high spatial resolution (FWHM $\sim 0''.14$ ) observations of the CO(8–7) line in GDS-14876, a compact star-forming galaxy at  $z = 2.3$  with total stellar mass of  $\log(M_{\star}/M_{\odot}) = 10.9$ . The spatially resolved velocity map of the inner  $r \lesssim 1$  kpc reveals a continuous velocity gradient consistent with the kinematics of a rotating disk with  $v_{\text{rot}}(r = 1\text{ kpc}) = 163 \pm 5$  km s<sup>-1</sup> and  $v_{\text{rot}}/\sigma \sim 2.5$ . The gas-to-stellar ratios estimated from CO(8–7) and the dust continuum emission span a broad range,  $f_{\text{gas}}^{\text{CO}} = M_{\text{gas}}/M_{\star} = 13 - 45\%$  and  $f_{\text{gas}}^{\text{cont}} = 50 - 67\%$ , but are nonetheless consistent given the uncertainties in the conversion factors. The dynamical modeling yields a dynamical mass of  $\log(M_{\text{dyn}}/M_{\odot}) = 10.58^{+0.5}_{-0.2}$  which is lower, but still consistent with the baryonic mass,  $\log(M_{\text{bar}} = M_{\star} + M_{\text{gas}}^{\text{CO}}/M_{\odot}) = 11.0$ , if the smallest CO-based gas fraction is assumed. Despite a low, overall gas fraction, the small physical extent of the dense, star-forming gas probed by CO(8–7),  $\sim 3\times$  smaller than the stellar size, implies a strong relative concentration that increases the gas fraction up to  $f_{\text{gas}}^{\text{CO}, 1\text{ kpc}} \sim 85\%$  in the central 1 kpc. Such a gas-rich center, coupled with a high star-formation rate,  $\text{SFR} \sim 500 M_{\odot} \text{ yr}^{-1}$ , suggests that GDS-14876 is quickly assembling a dense stellar component (*bulge*) in a strong nuclear starburst. Assuming its gas reservoir is depleted without replenishment, GDS-14876 will quickly ( $t_{\text{depl}} \sim 27$  Myr) become a compact quiescent galaxy that could retain some fraction of the observed rotational support.

*Subject headings:* galaxies: photometry — galaxies: high-redshift

### 1. INTRODUCTION

Compact star-forming galaxies (SFGs) are frequently referred to as a population of massive, strongly star-forming galaxies at  $z \gtrsim 2$  whose small sizes and high stellar mass concentrations (e.g., Wuyts et al. 2011; Barro et al. 2013) closely resemble those of typical quiescent galaxies of the same mass and redshift (e.g., Daddi et al. 2005; Trujillo et al. 2007). These galaxies have been identified in sizable numbers and their properties: small stellar sizes, steep radial mass profiles and obscured SFR properties have all been confirmed by multiple studies (e.g., Barro et al. 2014a; van Dokkum et al. 2015). Moreover, NIR spectroscopic follow-up has allowed a characterization of the kinematic and dynamical properties of their ionized gas from the analysis of rest-frame optical emission lines (e.g., Barro et al. 2014b; van Dokkum et al. 2015; Nelson et al. 2016). These initial results revealed high integrated velocity dispersions ( $\sigma \gtrsim 200$  km s<sup>-1</sup>) and large dynamical masses, roughly consistent with their stellar masses, which imply relatively low gas (and dark matter) fractions, and short depletion times. All this evidence is consistent with the

evolutionary picture in which compact SFGs are in a short-lived starburst phase, triggered by a dissipative event, which leads to the rapid formation of a compact core and subsequent quenching into a compact quiescent galaxy (e.g.; Zolotov et al. 2015; Wellons et al. 2015).

Nonetheless, tension with the dynamical constraints emerged when further spectroscopic follow-up of compact SFGs revealed that at least 20% have dynamical masses that are up to  $10\times$  lower than their stellar masses (van Dokkum et al. 2015). The most likely explanation for such large discrepancies are the uncertainties on the dynamical modeling assumptions. For example, the line-of-sight inclination, the ratio between ordered and random motions of the gas (i.e., the amount of rotational support,  $v_{\text{rot}}/\sigma$ ), the extent of gas profile relative to the stellar mass distribution, or the aperture corrections to scale the measurements within the slit to either galaxy-wide or effective ( $r = r_e$ ) values can all contribute to the observed difference (e.g., van Dokkum et al. 2015; Price et al. 2016).

A way to reduce these uncertainties is obtaining emission line velocity maps with similar or better spatial resolution than the stellar mass maps derived from Hubble Space Telescope (HST) data (e.g., Wuyts et al. 2012). These resolved maps can trace the kinematic properties of the gas and allow a more precise dynamical modeling by comparing the gas and stellar mass profiles at a similar scale. The high spatial resolution of sub-mm spectroscopy with Atacama Large Millimeter/sub-millimeter Array (ALMA) and the Karl G. Jansky Very Large Array (VLA) are a perfect match for this analysis. Sub-mm observations are insensitive to the dust obscuration that heavily attenuates optical emission lines, and provide not

<sup>1</sup> University of the Pacific, USA

<sup>2</sup> University of California Berkeley, USA

<sup>3</sup> Universidad Complutense de Madrid, Spain

<sup>4</sup> Universidad Diego Portales, Chile

<sup>5</sup> Max Planck Institute for Extraterrestrial Physics, Germany

<sup>6</sup> Chulalongkorn University, Thailand

<sup>7</sup> National Astronomical Research Institute of Thailand

<sup>8</sup> Kavli Institute for Physics and Mathematics, Japan

<sup>9</sup> University of California Santa Cruz, USA

<sup>10</sup> The Hebrew University, Israel

<sup>11</sup> Santa Cruz Institute for Particle Physics, USA

<sup>12</sup> Colby College, USA

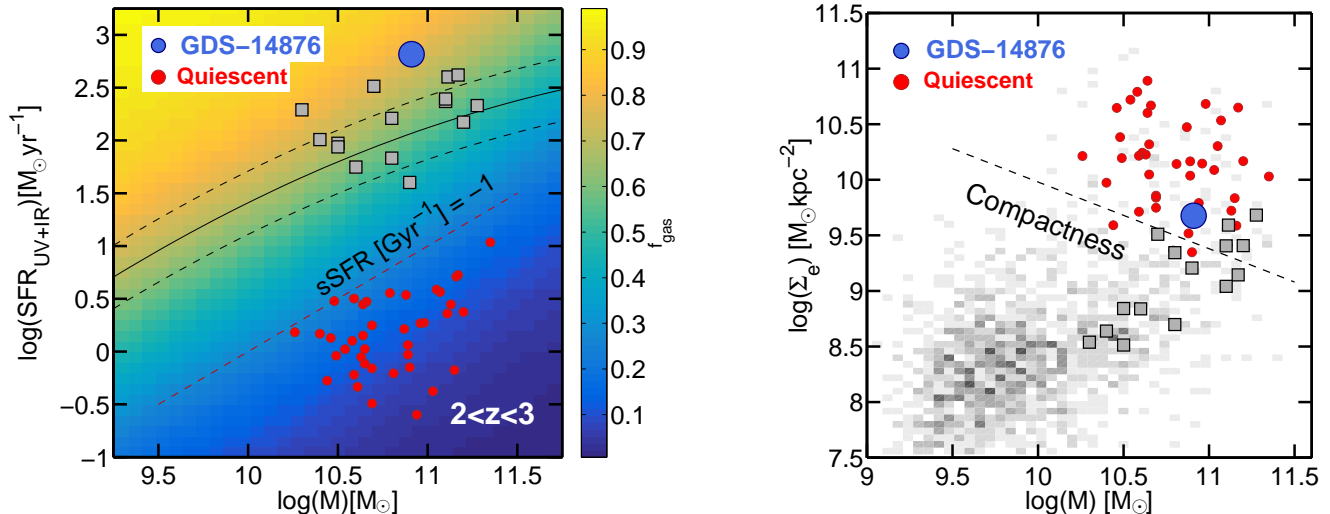


FIG. 1.— *Left*: Logarithm of SFR vs. stellar mass for GDS-14876 (blue circle) and other massive SFGs at  $z \sim 2$  (grey squares) observed with ALMA and HST, drawn from Spilker et al. (2016), Rujopakarn et al. (2016) and Popping et al. (2017). The black lines show the locus and  $\times 5$  limits (solid and dashed) of the SFR sequence at  $z = 2.25$  from Whitaker et al. (2014). The background is colored by the predicted gas fraction determined from the empirical prediction of Genzel et al. (2015). GDS-14876 lies above the SFR sequence and is expected to have a large  $f_{\text{gas}} \sim 80\%$ . The red line and circles show the location of the quiescent population at the same redshift, selected by low  $s\text{SFR} < -1 \text{ Gyr}^{-1}$ . *Right*: Logarithm of the effective mass surface density vs. stellar mass for galaxies in CANDELS-GDS at  $z \sim 2$  (greyscale) and all galaxies from the left panel. The dashed line indicates the compactness selection criterion of Barro et al. (2017).

only resolved kinematics from CO and carbon lines (e.g., Tadaki et al. 2017; Popping et al. 2017), but also far IR continuum detections to characterize the SFR and the baryonic content (i.e., gas and stars) of the galaxies (e.g.; Scoville et al. 2016; Rujopakarn et al. 2016).

This work presents CO J=8–7 line and sub-mm continuum observations of a compact SFG at  $z = 2.3$  using ALMA. From the joint analysis of the high spatial resolution HST/ACS, HST/WFC3 and ALMA continuum and CO line imaging, we simultaneously characterize the spatial distribution and kinematics of the molecular gas. Throughout this paper, we quote magnitudes in the AB system, assume a Chabrier (2003) initial mass function, and adopt the following cosmological parameters:  $(\Omega_M, \Omega_\Lambda, h) = (0.3, 0.7, 0.7)$ .

## 2. TARGET SELECTION AND OBSERVATIONS

The galaxy analyzed in this paper is drawn from the compact SFGs sample in the CANDELS (Grogin et al. 2011) GOODS-S region presented in Barro et al. (2014a, 2016). The panels in Figure 1 summarize the selection criteria in SFR and compactness. Figure 2 shows the UV to near-IR spectral energy distribution (SED), which includes extensive multi-band data ranging from U to  $8\mu\text{m}$  (Guo et al. 2013). Furthermore, we include far-IR data from Spitzer MIPS (Pérez-González et al. 2008), Herschel PACS and SPIRE from the GOODS-Herschel survey (Elbaz et al. 2011), and VLA 21 cm and 5 cm maps (Kellermann et al. 2008; Rujopakarn et al. 2016). The stellar population properties are determined by fitting the optical & NIR SED using FAST (Kriek et al. 2009), assuming Bruzual & Charlot (2003) stellar population synthesis models, an exponentially-declining star formation history, and the Calzetti et al. (2000) dust law with attenuation  $0 < A_V < 4$ , yielding  $\log(M_*/M_\odot) = 10.9$ . The SFR was determined in Barro et al. (2016) from a combination of rest-frame UV and IR SFR indicators and modeling the far-IR emission with dust-emission templates, yielding  $\log(\text{SFR}/M_\odot \text{ yr}^{-1}) = 2.7$ .

The sub-mm observations of GDS-14876 were taken as part of an ALMA cycle-3 campaign (ID: 2015.1.00907.S; PI: G. Barro) to study CO emission lines in compact SFGs at  $z = 2 - 3$ . The observations were conducted on 2016-09-17 in band 7 using four spectral windows in the largest bandwidth mode. The on-source integration time was 51 min in an extended array configuration, C39-7 (shortest and longest baselines were 15.1 m and 3.1 km, respectively). The water vapor during the observations was PWV = 0.5 mm. Flux, phase, and band-pass calibrators were also obtained, for a total time of  $\sim 2$  hr. All the correlators were set to a bandwidth of 1.875 GHz covering 128 channels. The reference spectral window (spw0) was centered at 278.57 GHz to target the CO(8-7) emission line, assuming the redshift derived from optical lines ( $z = 2.309$ ). The other spectral windows were centered at 276.91, 288.91, and 290.91 GHz. These spectral windows were used to observe the band 7 continuum of the target.

We use the CASA software (McMullin et al. 2007) to process and clean the data. We use the tclean task with natural weighting for the u-v visibility plane. This resulted in a synthetic beam size with an average angular resolution of  $\text{FWHM} = 0''.14 \times 0''.12$  ( $1.15 \times 0.98$  kpc), with a major-axis position angle (P.A.) of  $70^\circ$ . The r.m.s. noise of the observations is  $0.19 \text{ mJy/beam}$  for the CO(8-7) line, measured in  $20 \text{ m s}^{-1}$  channel bins, and  $\sigma = 28 \mu\text{Jy/beam}$  or  $1.5 \text{ mJy/arcsec}^2$  for the continuum, measured on the clean continuum maps excluding the frequency range of the CO line.

## 3. STRUCTURAL PROPERTIES

Figure 2 shows the WFC3/ACS color-composite image of the galaxy as well as the ALMA 1.1 mm continuum emission and CO(8-7) velocity maps. We measure the structural properties of GDS-14876 in the F160W image, which at  $z = 2.3$  traces the rest-frame optical emission, using GALFIT (Peng et al. 2010) assuming a single

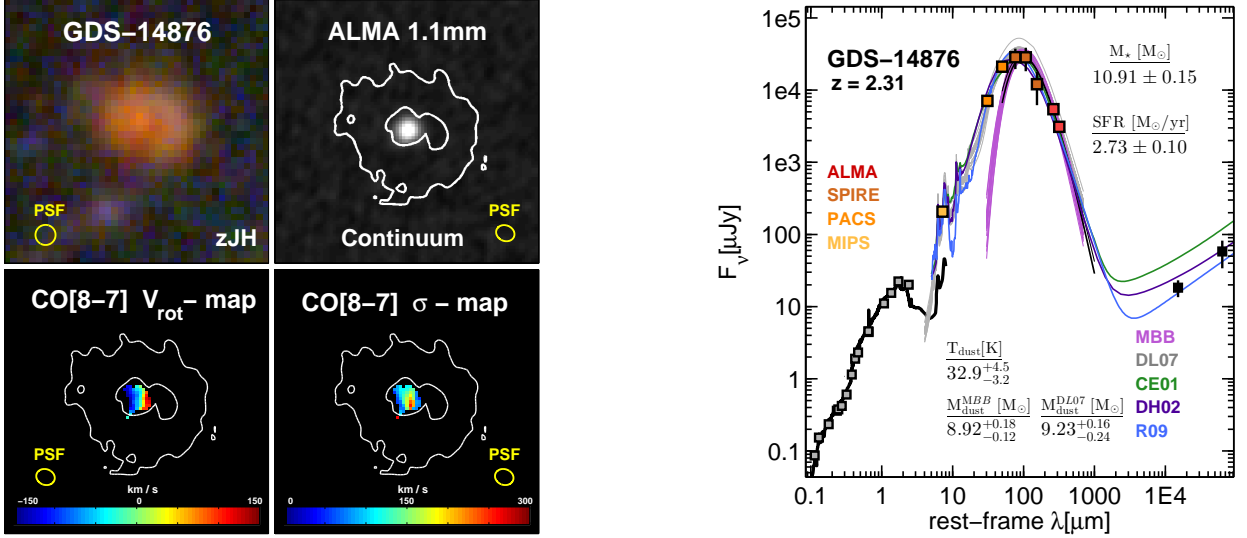


FIG. 2.— *Left:* From top to bottom,  $2''.5 \times 2''.5$  ( $20 \times 20$  kpc) images of GDS-14876 in WFC3/F160W and ALMA 870  $\mu\text{m}$ , and CO(8 – 7) rotation velocity and dispersion maps at the same physical scale (with the F160W contours shown in white). *Right:* UV-to-FIR SED of GDS-14876. The black line show the best-fit BC03 stellar population model for the photometry up to 8  $\mu\text{m}$  rest-frame (gray squares). The orange-to-red and black squares show the mid-to-far IR photometry and radio data. The green, purple and blue lines show the best-fit dust emission models from the libraries of Chary & Elbaz (2001), Dale & Helou (2002) and Rieke et al. (2009). The grey and pink regions depict 300 models drawn from the posterior probability distribution of the fit to the Draine & Li (2007) models and to a MBB model, respectively. The median values and confidence intervals for  $M_{\text{dust}}$  and  $T_{\text{dust}}$  are indicated.

two-dimensional Sérsic profile. We obtain size and Sérsic index values of  $r_e = 2.3 \pm 0.1$  kpc and  $n = 0.6$ . The total (99%) isophotal size is  $r_{\text{tot}} = 8.25 \pm 0.04$  kpc (outer white contours in Figure 2).

Following Barro et al. (2016), we use GALFIT and the synthetic PSF of the ALMA beam to compute the size and Sérsic index of the continuum emission, obtaining values of  $r_e = 0.74 \pm 0.04$  kpc,  $n = 1.6$ . To measure the structural properties of the CO emission line region, we subtract the continuum flux from the image using CASA’s `uvsubcont` task and then collapse the resulting data-cube in velocity space using a  $\pm 250$  km/s bin around the central wavelength of the CO[8-7] line. Lastly, we run GALFIT on the resulting image, obtaining values of  $r_e = 0.67 \pm 0.05$  kpc and  $n = 0.9$ .

Both the continuum and emission line sizes are  $\sim 3 \times$  smaller than the rest-frame optical size (Figure 2). This is consistent with previous results based on dust continuum measurements (e.g., Barro et al. 2016; Tadaki et al. 2015; Rujopakarn et al. 2016), which suggest that the compact CO and far-IR emission trace a strong nuclear starburst. This compact burst contrasts with the typical inside-growth of star-forming galaxies in which gas profiles are more extended than the stellar distribution (e.g., Nelson et al. 2016). We note however that given the high order CO transition, it is possible that ALMA only detects the region where  $J = 8 - 7$  can be excited, i.e., a dense and strongly ionized region in the center.

#### 4. DUST AND GAS MASSES

##### 4.1. Continuum-based measurement

We fit the mid-to-FIR SED using different libraries of dust emission templates (e.g., Chary & Elbaz 2001, Dale & Helou 2002) to estimate the total IR luminosity and SFR (see Figure 2). In addition, we fit to the models by Draine & Li (2007, DL07) and to a set of modified black body models (MBB, e.g., Casey et al. 2012) to estimate the dust temperature and dust mass of the galaxy.

The best-fit models and the corresponding confidence intervals are computed by exploring the parameter space using the Python Markov-Chain Monte Carlo package `emcee` (Foreman-Mackey et al. 2013). The MBB fit assumes an average dust emissivity of  $\kappa = 1 \text{ cm}^2\text{g}^{-1}$  at 850  $\mu\text{m}$  (e.g., Dunne et al. 2003; Scoville et al. 2016) and a range of  $\beta = 1.5 - 2.5$ . Both estimates of the dust mass are roughly consistent within the errors. The DL07 models yield a value of  $\log(M_{\text{dust}}^{\text{DL07}}/M_\odot) = 9.2 \pm 0.3$ , while the MBB models with best-fit values  $\beta \sim 1.5$  and  $T = 33$  K provide a slightly lower value of  $\log(M_{\text{dust}}^{\text{MBB}}/M_\odot) = 8.9 \pm 0.2$ . Based on these  $M_{\text{dust}}$  values, we estimate the molecular gas content using the gas-to-dust ratio by assuming  $\delta_{\text{GDR}} M_{\text{dust}} = M_{\text{H}_2} + M_{\text{HI}} \sim M_{\text{H}_2}$ . The value of  $\delta_{\text{GDR}}$  depends primarily on the metallicity of the galaxy (e.g., Sandstrom et al. 2013). Here we assume the typical value for solar metallicity,  $\delta_{\text{GDR}} \sim 100$ . This leads to gas masses of  $\log(M_{\text{gas}}^{\text{DL07}}/M_\odot) = 11.2 \pm 0.3$  and  $\log(M_{\text{gas}}^{\text{MBB}}/M_\odot) = 10.9 \pm 0.2$  dex. Lower values of the metallicity would yield larger gas masses.

##### 4.2. CO-based measurement

We estimate the gas mass from the CO(8 – 7) line luminosity using

$$L'_{\text{CO}} [\text{K km s}^{-1} \text{pc}^2] = 3.25 \times 10^7 (S_{\text{CO}} \Delta v) \frac{D_L^2}{(1+z)^3 \nu_{\text{obs}}^2} \quad (1)$$

where  $S_{\text{CO}} \Delta v$  is the line flux and  $D_L$  is the luminosity distance. We obtain  $\log L'_{\text{CO},8-7} = 9.65 \pm 0.17$  dex. From  $L'_{\text{CO}}$ , we estimate the total mass of molecular hydrogen as  $\log(M_{\text{gas}}/M_\odot) = \log(\alpha_{\text{CO}} L'_{\text{CO},J}/R_{J,1})$ , where  $R_{J,1} = [S_J/S(1-0)]/J^2$  is the conversion factor to correct for the lower Rayleigh-Jeans brightness temperature of the  $J = 8 - 7$  transition relative to  $1 - 0$ , and  $\alpha_{\text{CO}}$  is the CO-to-H<sub>2</sub> conversion factor. For the  $J = 8 - 7$  transition the conversion factor is relatively unconstrained,

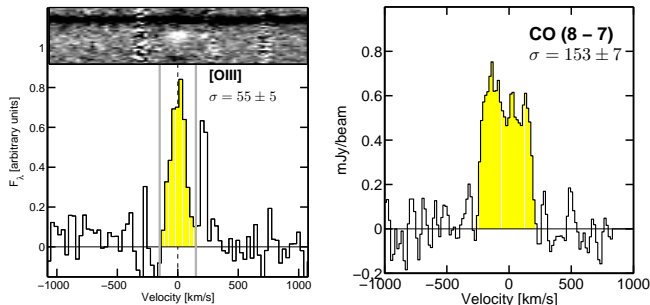


FIG. 3.— *Left*: MOSFIRE H-band spectra of GDS-14876 showing the 2D and collapsed 1D profile of the [OIII] emission line. The grey lines indicate  $\pm 150 \text{ km s}^{-1}$  for reference. *Right*: Continuum-subtracted spectral profile of the CO(8-7) line extracted from the ALMA image using a  $0''.3$  diameter circular aperture. At face-value, the dispersion of the CO line, measured from a single Gaussian fitting, is  $\sim 3\times$  larger than that of the optical [OIII] line.

e.g.,  $R_{8,1} = 0.9$  (Bradford et al. 2009),  $R_{8,1} = 0.01 - 0.4$  (Danielson et al. 2013; Kamenetzky et al. 2016). Here we adopt a conservative value of  $R_{8,1} = 0.30 \pm 0.20$ , where the more sub-thermally excited is the gas ( $R_{8,1} \ll 1$ ), or the lower is the ISM density, the higher is the gas mass (see e.g., Daddi et al. 2015). The value of  $\alpha_{\text{CO}}$  also depends on the physical conditions of the ISM. Adopting  $\alpha_{\text{CO}} = 0.8 M_{\odot} (\text{K km s}^{-1} \text{ pc}^2)^{-1}$ , the typical value for nearby ultra-luminous infrared galaxies and SMGs (e.g., Tacconi et al. 2008), we obtain  $\log(M_{\text{gas}}^{\text{SMG}}/M_{\odot}) = 10.08^{+0.30}_{-0.18}$  dex. If we use the larger Milky Way CO-to- $\text{H}_2$  conversion,  $\alpha_{\text{CO}} = 4.3 M_{\odot} (\text{K km s}^{-1} \text{ pc}^2)^{-1}$ , the resulting gas mass is  $\log(M_{\text{gas}}^{\text{MW}}/M_{\odot}) = 10.81^{+0.30}_{-0.18}$  dex.

In summary, different indicators yield values of the dense, star-forming gas mass that may differ up to  $\sim 1$  dex, nonetheless, given the wide range of modeling assumptions and uncertainties in the conversion factors, these values are still consistent. In Section §6 we discuss which of these estimates is more consistent with the dynamical constraints. The estimates based on the CO line provide a lower limit and imply gas fractions of  $f_{\text{gas}}^{\text{CO}} \sim 13^{+10}_{-4}\%$  to  $45^{+17}_{-10}\%$  for the SMG and MW gas-to-mass conversions, respectively. The dust continuum based values computed with either the MBB or DL07 models yield higher gas fractions of  $f_{\text{gas}}^{\text{cont}} = 50 \pm 11\%$  to  $67 \pm 15\%$ , respectively.

Note that these fractions refer to the total, integrated masses. The spatially resolved gas-to-stellar ratio within the region detected in CO ( $r \lesssim 1 \text{ kpc}$ ) is much larger, even for the relatively modest CO-based gas masses,  $f_{\text{gas}}^{\text{CO}, 1 \text{ kpc}} = 85\%$ . This value indicates that GDS-14876 has a gas-rich nuclear region that fuels the similarly compact starburst detected in the dust continuum emission. Assuming no replenishment, the depletion time of this burst is very short:  $t_{\text{depl}} = \text{SFR}/M_{\text{gas}}^{\text{CO, SMG}} = 27 \pm 12 \text{ Myr}$ .

## 5. KINEMATICS AND DYNAMICAL MODELING

### 5.1. [OIII] kinematics

GDS-14876 was observed using the NIR multi-object spectrograph MOSFIRE (McLean et al. 2010) on Keck-I. A full description of the observations and data reduction is presented in Barro et al. (2014b). The spectrum yields a clear ( $> 5\sigma$ ) detection of the [OIII]  $5007\text{\AA}$  line

(left panel Figure 3), while the  $\text{H}\beta$  line is undetected ( $[\text{OIII}]/\text{H}\beta \gtrsim 0.8$ ). The [OIII] profile is relatively narrow with a  $\sigma = 55 \pm 5 \text{ km s}^{-1}$ .

### 5.2. CO kinematics

Figure 4 shows the observed rotation velocity and dispersion fields for GDS-14876 obtained by fitting the CO emission line at every spaxel with a single Gaussian. The velocity field reveals a continuous shear and a central dispersion peak which are consistent with the kinematics of a rotating disk. Assuming that the gas is gravitationally bound in a disk, we model the observed kinematic profile to characterize the dynamical properties of the galaxy.

First, we measure the integrated dispersion of the galaxy by fitting a single Gaussian to the spectrum extracted with a  $0''.3$  diameter circular aperture. The integrated  $\sigma = 153 \pm 7 \text{ km s}^{-1}$  (right panel of Figure 3) is almost  $3\times$  larger than the dispersion inferred from [OIII]. Such a large difference could indicate that the ionized and neutral gas trace distinct physical regions (e.g., if [OIII] traces a relatively unobscured, coronal layer of the star-forming region). The misalignment of the MOSFIRE slit relative to the kinematic major axis (magenta vs. white slit in leftmost panel of Figure 4) can also lower the dispersion. However, the linewidth measured on a CO spectrum extracted along the MOSFIRE slit PA after convolving the ALMA cube to a  $\text{FWHM} = 0''.7$  resolution still yields a much larger  $\sigma \gtrsim 100 \text{ km s}^{-1}$ , and suggests that this effect is only minor.

Next, we analyze the spatially-resolved velocity field using a forward dynamical modeling procedure which fits the velocity profiles in observed space. The 1D spectra are extracted along the kinematic major axis using circular apertures with a diameter equal to the FWHM of the observations. The dynamical model assumes that the ionized gas is rotating in a thin disk, and that the disk density profile can be described by a Freeman model (Freeman 1970). We account for the effects of pressure support by lowering the rotation velocity following Wuyts et al. (2016, and references therein). The fit includes the effects of beam smearing ( $\text{FWHM} = 0''.14 \times 0''.12$ ), and the line-of-sight inclination. We estimate the latter from the optical axis-ratio,  $q = 0.82$ , following the method of van Dokkum et al. (2015), and we obtain  $i = 62^{+8}_{-15}$ .

The free parameters of the dynamical fit are three: the total dynamical mass and effective radius of the disk,  $M_{\text{dyn}}$  and  $r_{\text{e}}^{\text{dyn}}$ , and the intrinsic dispersion floor,  $\sigma_0$ , measured at large radii. Figure 4 shows the observed rotation and dispersion measurements, extracted along a pseudo slit, compared to the best-fit model. The best-fit values of  $M_{\text{dyn}}$  and  $r_{\text{e}}^{\text{dyn}}$  exhibit a positive correlation with  $1\sigma$  confidence regions of  $r_{\text{e}}^{\text{dyn}} = 1.7^{+0.5}_{-0.4} \text{ kpc}$  and  $\log(M_{\text{dyn}}/M_{\odot}) = 10.58^{+0.52}_{-0.20}$ , where the largest radius corresponds to the largest mass. Note that the inner 1 kpc is very well constrained by the models. However, the turnover radius is only loosely constrained because the CO tracer (magenta), probes a smaller region than the confidence interval for  $r_{\text{e}}^{\text{dyn}}$  (grey region).

The best-fit model yields also an intrinsic  $\sigma_0 = 73 \pm 8 \text{ km s}^{-1}$  and a rotation velocity at  $r = 1 \text{ kpc}$  of  $v_{\text{rot}} \sin i = 163 \pm 5 \text{ km s}^{-1}$ . The dispersion value is slightly higher but consistent with the typi-

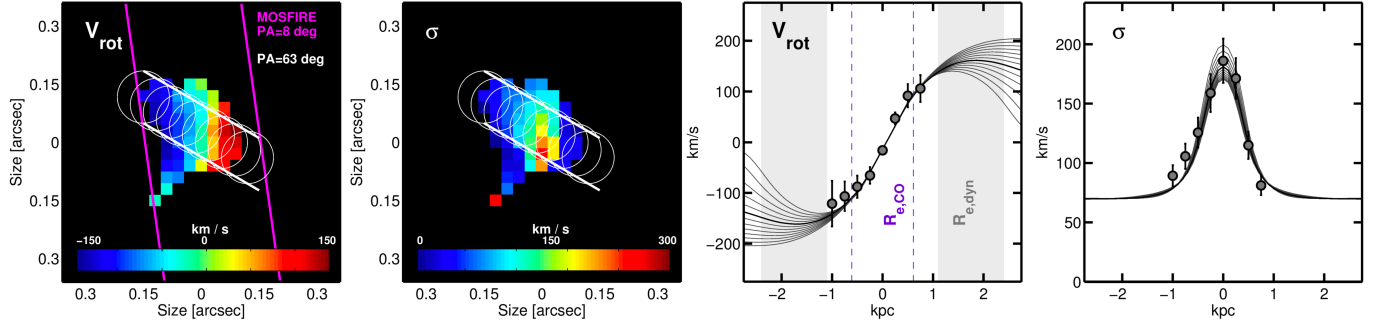


FIG. 4.— *Left*: Moment maps of the central region of GDS-14876 showing the projected CO velocity field and velocity dispersion where  $S/N \geq 3$ . The white circles marking the extracted pseudo slit using apertures with the FWHM of the minimum resolution element. The magenta lines illustrate the orientation of the slit in the MOSFIRE [OIII] observations, which is misaligned with the CO kinematic major axis by  $\sim 50^\circ$ . *Right*: Observed (grey circles) and best-fit models (black line and  $1\sigma$  grey) for the rotation velocity and velocity dispersion profiles along the kinematic major axis. The dynamical modeling of the kinematic maps is consistent with a rotating disk of gas. The dashed lines and grey regions indicate the CO effective radius and the  $1\sigma$  confidence for  $r_e^{\text{dyn}}$ .

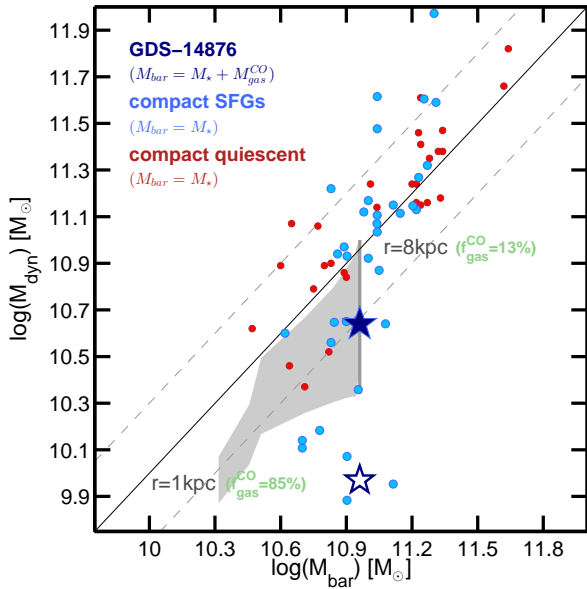


FIG. 5.— Comparison between the dynamical and stellar masses for GDS-14876 and other samples of compact SFGs (blue) and quiescent (red) galaxies from Barro et al. (2014b), van Dokkum et al. (2015), van de Sande et al. (2013) and Belli et al. (2014). The blue stars show  $M_{\text{dyn}}$  for GDS-14876 as computed from the CO (filled) and [OIII] (empty) lines. The grey shaded area depicts the confidence region of the comparison between cumulative  $M_{\text{dyn}}$  and  $M_*$  with increasing radii from  $r = 1$  kpc to  $r = 8$  kpc (i.e., total mass). The CO-based gas fraction at both ends is indicated.  $M_{\text{dyn}}$  and  $M_{\text{bar}}$  are consistent within the confidence range, although the latter lies predominantly in the unphysical region,  $M_{\text{bar}} > M_{\text{dyn}}$ .

cal range observed in massive SFGs at  $z \sim 2$  (e.g., Wisnioski et al. 2015; Price et al. 2016; Tadaki et al. 2017). The  $v_{\text{rot}}/\sigma_0 \sim 2.5$ , also indicates that the disk is rotation dominated.

## 6. DISCUSSION

Figure 5 compares the baryonic (assuming  $M_{\text{gas}}=0$ , i.e.,  $M_{\text{bar}}=M_*$ ) and dynamical masses for a sample of massive, compact SFGs and quiescent galaxies at  $z \gtrsim 2$  from the literature. Most galaxies exhibit a relatively good agreement within the usual  $\sim 0.3$  dex scatter (dashed line). However, there is a group of compact SFG outliers with low  $M_{\text{dyn}}$  and  $M_{\text{dyn}}/M_{\text{bar}} \ll 1$ . These outliers, found by van Dokkum et al. (2015), have small integrated dispersions in their optical emission lines, which

leads to small dynamical masses,  $M_{\text{dyn}} \propto \sigma^2 r_e$ . GDS-14876 exhibits a similar issue, i.e., the dynamical mass computed using  $\sigma([\text{OIII}])=55$  km/s is almost  $10\times$  smaller than its baryonic mass (empty star) even for the smallest fraction of dense, star-forming gas,  $f_{\text{gas}}^{\text{CO}} \sim 13\%$ .

The  $M_{\text{dyn}}$  value inferred from the dynamical modeling of the CO emission line provides a better agreement between total  $M_{\text{dyn}}$  and  $M_{\text{bar}}$ , although the latter is still in the unphysical region (filled star). As discussed in the previous section, this tension decreases for larger values of the  $r_e^{\text{dyn}}$  (or the line-of-sight inclination) which could be better constrained by probing further out into the rotation curve, possibly by observing lower-order CO transitions which are sensitive to colder and potentially more extended neutral gas. Nevertheless, the comparison between total  $M_{\text{dyn}}$  and  $M_{\text{bar}}$  suggests that the galaxy is strongly baryon dominated, and the small consistency margin between the two masses favors the lowest CO-based gas fraction to avoid strongly unphysical results with  $M_{\text{dyn}}/M_{\text{bar}} \ll 1$ . A low overall gas fraction also agrees with similarly low values reported in recent studies of compact SFGs (Spilker et al. 2016; Tadaki et al. 2015; Popping et al. 2017) and leaves little room for a colder and more extended gas component that might be undetected by the high order CO(8–7) emission.

he spatially-resolved evolution of the  $M_{\text{dyn}}/M_*(r \leq R)$  ratio from  $R = 1$  kpc to  $R = 8$  kpc exhibits a similar result. The shaded grey region in Figure 5 shows that the tension with  $M_{\text{dyn}}$  increases towards the central region, where the stronger concentration of star-forming gas relative to stars ( $\sim 3\times$  smaller size) increases the gas fraction to  $f_{\text{gas}}^{\text{CO}, 1\text{kpc}} \sim 85\%$ . Note, however, that while dynamical model is better constrained in the center (narrower grey region) the stellar mass within 1 kpc is likely more uncertain because the large central obscuration and limited spatial resolution can both bias the SED-fitting based stellar mass estimate, particularly for such a small, compact galaxy.

In summary, the emerging picture from the CO and dust-continuum based measurements suggests that GDS-14876 is having a compact and likely short-lived nuclear starburst that could lead to the rapid formation of a compact quiescent galaxy. A relevant prediction of the kinematic modeling is that such quiescent descendant could preserve some of the observed rotational support, as al-

ready hinted by recent observations (e.g., Newman et al. 2015; Toft et al. 2017).

#### ACKNOWLEDGMENTS

GB and MK acknowledge support from HST-AR-12847 and HST-AR-14552. PGP-G acknowledge support from grants AYA2015-63650-P and AYA2015-70815-ERC. W.R. is supported by JSPS KAKENHI Grant Number JP15K17604 and the Thailand Research Fund/Office of the Higher Education Commission Grant

Number MRG6080294. This paper makes use of the following ALMA data: ADS/JAO.ALMA#2015.1.00907.S. ALMA is a partnership of ESO (representing its member states), NSF (USA) and NINS (Japan), together with NRC (Canada), NSC and ASIAA (Taiwan), and KASI (Republic of Korea), in cooperation with the Republic of Chile. The Joint ALMA Observatory is operated by ESO, AUI/NRAO and NAOJ. The National Radio Astronomy Observatory is a facility of the National Science Foundation operated under cooperative agreement by Associated Universities, Inc.

#### REFERENCES

- Barro, G., Faber, S. M., Koo, D. C., et al. 2017, *ApJ*, 840, 47
- Barro, G., Faber, S. M., Pérez-González, P. G., et al. 2013, *ApJ*, 765, 104
- . 2014a, *ApJ*, 791, 52
- Barro, G., Kriek, M., Pérez-González, P. G., et al. 2016, *ApJ*, 827, L32
- Barro, G., Trump, J. R., Koo, D. C., et al. 2014b, *ApJ*, 795, 145
- Belli, S., Newman, A. B., Ellis, R. S., et al. 2014, *ApJ*, 788, L29
- Bradford, C. M., Aguirre, J. E., Aikin, R., et al. 2009, *ApJ*, 705, 112
- Bruzual, G., & Charlot, S. 2003, *MNRAS*, 344, 1000
- Calzetti, D., Armus, L., Bohlin, R. C., et al. 2000, *ApJ*, 533, 682
- Casey, C. M., Berta, S., Béthermin, M., et al. 2012, *ApJ*, 761, 140
- Chabrier, G. 2003, *PASP*, 115, 763
- Chary, R., & Elbaz, D. 2001, *ApJ*, 556, 562
- Daddi, E., Dannerbauer, H., Liu, D., et al. 2015, *A&A*, 577, A46
- Daddi, E., Renzini, A., Pirzkal, N., et al. 2005, *ApJ*, 626, 680
- Dale, D. A., & Helou, G. 2002, *ApJ*, 576, 159
- Danielson, A. L. R., Swinbank, A. M., Smail, I., et al. 2013, *MNRAS*, 436, 2793
- Draine, B. T., & Li, A. 2007, *ApJ*, 657, 810
- Dunne, L., Eales, S., Ivison, R., et al. 2003, *Nature*, 424, 285
- Elbaz, D., Dickinson, M., Hwang, H. S., et al. 2011, *A&A*, 533, A119
- Foreman-Mackey, D., Hogg, D. W., Lang, D., et al. 2013, *PASP*, 125, 306
- Freeman, K. C. 1970, *ApJ*, 160, 811
- Genzel, R., Tacconi, L. J., Lutz, D., et al. 2015, *ApJ*, 800, 20
- Grogin, N. A., Kocevski, D. D., Faber, S. M., et al. 2011, *ApJS*, 197, 35
- Guo, Y., Ferguson, H. C., Giavalisco, M., et al. 2013, *ApJS*, 207, 24
- Kamenetzky, J., Rangwala, N., Glenn, J., et al. 2016, *ApJ*, 829, 93
- Kellermann, K. I., Fomalont, E. B., Maimieri, V., et al. 2008, *ApJS*, 179, 71
- Kriek, M., van Dokkum, P. G., Labbé, I., et al. 2009, *ApJ*, 700, 221
- McLean, I. S., Steidel, C. C., Epps, H., et al. 2010, in *Proc. SPIE*, Vol. 7735, Ground-based and Airborne Instrumentation for Astronomy III, 77351E–77351E–12
- McMullin, J. P., Waters, B., Schiebel, D., et al. 2007, in *Astronomical Society of the Pacific Conference Series*, Vol. 376, *Astronomical Data Analysis Software and Systems XVI*, ed. R. A. Shaw, F. Hill, & D. J. Bell, 127
- Nelson, E. J., van Dokkum, P. G., Förster Schreiber, N. M., et al. 2016, *ApJ*, 828, 27
- Newman, A. B., Belli, S., & Ellis, R. S. 2015, *ApJ*, 813, L7
- Peng, C. Y., Ho, L. C., Impey, C. D., et al. 2010, *AJ*, 139, 2097
- Pérez-González, P. G., Trujillo, I., Barro, G., et al. 2008, *ApJ*, 687, 50
- Popping, G., Decarli, R., Man, A. W. S., et al. 2017, *ArXiv e-prints*
- Price, S. H., Kriek, M., Shapley, A. E., et al. 2016, *ApJ*, 819, 80
- Rieke, G. H., Alonso-Herrero, A., Weiner, B. J., et al. 2009, *ApJ*, 692, 556
- Rujopakarn, W., Dunlop, J. S., Rieke, G. H., et al. 2016, *ApJ*, 833, 12
- Sandstrom, K. M., Leroy, A. K., Walter, F., et al. 2013, *ApJ*, 777, 5
- Scoville, N., Sheth, K., Aussel, H., et al. 2016, *ApJ*, 820, 83
- Spilker, J. S., Bezanson, R., Marrone, D. P., et al. 2016, *ApJ*, 832, 19
- Tacconi, L. J., Genzel, R., Smail, I., et al. 2008, *ApJ*, 680, 246
- Tadaki, K.-i., Kodama, T., Nelson, E. J., et al. 2017, *ApJ*, 841, L25
- Tadaki, K.-i., Kohno, K., Kodama, T., et al. 2015, *ApJ*, 811, L3
- Toft, S., Zabl, J., Richard, J., et al. 2017, *Nature*, 546, 510
- Trujillo, I., Conselice, C. J., Bundy, K., et al. 2007, *MNRAS*, 382, 109
- van de Sande, J., Kriek, M., Franx, M., et al. 2013, *ApJ*, 771, 85
- van Dokkum, P. G., Nelson, E. J., Franx, M., et al. 2015, *ApJ*, 813, 23
- Wellons, S., Torrey, P., Ma, C.-P., et al. 2015, *MNRAS*, 449, 361
- Whitaker, K. E., Franx, M., Leja, J., et al. 2014, *ApJ*, 795, 104
- Wisnioski, E., Förster Schreiber, N. M., Wuyts, S., et al. 2015, *ApJ*, 799, 209
- Wuyts, S., Förster Schreiber, N. M., Genzel, R., et al. 2012, *ApJ*, 753, 114
- Wuyts, S., Förster Schreiber, N. M., van der Wel, A., et al. 2011, *ApJ*, 742, 96
- Wuyts, S., Förster Schreiber, N. M., Wisnioski, E., et al. 2016, *ApJ*, 831, 149
- Zolotov, A., Dekel, A., Mandelker, N., et al. 2015, *MNRAS*, 450, 2327